Correlations between age, kinematics, and chemistry as seen by the RAVE survey

Jennifer Wojno,[1,2]★ Georges Kordopatis,[3] Matthias Steinmetz,[1] Paul McMillan,[4] James Binney,[5] Benoit Famaey,[6] Giacomo Monari,[1] Ivan Minchev,[1] Rosemary F. G. Wyse,[2] Teresa Antoja,[7] Arnaud Siebert,[6] Ismael Carrillo,[1] Joss Bland-Hawthorn,[8] Eva K. Grebel,[9] Tomaž Zwitter,[10] Olivier Bienaymé,[6] Brad Gibson,[11] Andrea Kunder,[12] Ulisse Munari,[13] Julio Navarro,[14] Quentin Parker,[15] Warren Reid[16,17] and George Seabroke[18]

Affiliations are listed at the end of the paper

ABSTRACT

We explore the connections between stellar age, chemistry, and kinematics across a Galactocentric distance of $7.5 < R(\text{kpc}) < 9.0$, using a sample of $\sim$12 000 intermediate-mass (FGK) turn-off stars observed with the RAdial Velocity Experiment (RAVE) survey. The kinematics of this sample are determined using radial velocity measurements from RAVE, and parallax and proper motion measurements from the *Tycho–Gaia* Astrometric Solution (TGAS). In addition, ages for RAVE stars are determined using a Bayesian method, taking TGAS parallaxes as a prior. We divide our sample into young ($0 < \tau < 3$ Gyr) and old ($8 < \tau < 13$ Gyr) populations, and then consider different metallicity bins for each of these age groups. We find significant differences in kinematic trends of young and old, metal-poor and metal-rich, stellar populations. In particular, we find a strong metallicity dependence in the mean Galactocentric radial velocity as a function of radius ($\partial V_{\rm R}/\partial R$) for young stars, with metal-rich stars having a much steeper gradient than metal-poor stars. For $\partial V_{\phi}/\partial R$, young, metal-rich stars significantly lag the LSR with a slightly positive gradient, while metal-poor stars show a negative gradient above the LSR. We interpret these findings as correlations between metallicity and the relative contributions of the non-axisymmetries in the Galactic gravitational potential (the spiral arms and the bar) to perturb stellar orbits.

Key words: Galaxy: kinematics and dynamics – solar neighbourhood – Galaxy: structure.

1 INTRODUCTION

The field of Galactic archaeology stands poised to reveal the formation history of our Galaxy. As low- and intermediate-mass stars are long-lived, they can act as time capsules, allowing us a window to the environment in which they were born (Freeman & Bland-Hawthorn 2002). Spectroscopic surveys, such as RAdial Velocity Experiment (RAVE; Steinmetz et al. 2006), SEGUE (Yanny et al. 2009), APOGEE (Majewski et al. 2017), *Gaia*-ESO (Gilmore et al. 2012), LAMOST (Zhao et al. 2012), and GALAH (De Silva et al. 2015), provide a number of crucial parameters necessary for disentangling the formation history of the Galactic disc, such as stellar radial velocities, effective temperatures, surface gravities, and individual chemical abundances. The precision with which we can exploit these spectra is being greatly increased by the progressive release of astrometric data from European Space Agency (ESA)'s *Gaia* satellite, starting with *Gaia* DR1 in September 2016 (Gaia Collaboration et al. 2016; Lindegren et al. 2016) and continuing with *Gaia* DR2 in April 2018.

It has been known for more than a century that the local velocity field is not uniform but contains moving groups (e.g. Proctor 1869; Kapteyn 1905)[1]: predominantly the Hyades, Pleiades, and Hercules groups. The precision of stellar velocity measurements in the solar neighbourhood has since increased dramatically, and as a result it is now possible to study this velocity space in fine detail (e.g. Dehnen 2000; Famaey, Siebert & Jorissen 2008; Williams et al.

★ E-mail: jwojno1@jhu.edu

[1]For a history of the discovery of moving groups see Antoja et al. (2010).

2013; Antoja et al. 2015, 2017; Kushniruk, Schirmer & Bensby 2017; Carrillo et al. 2018). These structures are indicative of deviations of the Milky Way (MW) disc from an idealized axisymmetric model associated with our Galaxy's bar and spiral arms. The way such structures vary in velocity space as a function Galactocentric radius has been explored in a number of simulations (e.g. Minchev et al. 2010; Antoja et al. 2011; Quillen et al. 2011; McMillan 2013; Monari et al. 2014, 2017), with a view to constraining the nature of the underlying non-axisymmetries. To understand better the dynamical processes that shape the kinematic trends we see in stellar populations today, we turn to measurements of the local mean stellar velocity field $\mathbf{V}$, which we analyse in Galactocentric cylindrical polar coordinates (R, ϕ, z).

Siebert et al. (2011) first detected a gradient in V_R, namely $\partial V_R / \partial R \lesssim -3 \, \mathrm{km \, s^{-1} \, kpc^{-1}}$, using the line-of-sight velocities of RAVE stars. Siebert et al. (2012) fitted this shallow gradient to a model on the assumption that it is solely due to long-lived spiral arms. They found that they were able to reproduce the observational results with a two-armed model in the solar neighbourhood ($d < 1 \, \mathrm{kpc}$), although they acknowledged that the bar could contribute. Monari et al. (2014) developed a model of the bar's contribution to the velocity field near the Sun. They showed that if the Sun is located close to the bar's outer Lindblad resonance (OLR), from our position we would measure a trend similar to that found in Williams et al. (2013), which measured a slightly steeper gradient, $\partial V_R / \partial R = -8 \, \mathrm{km \, s^{-1} \, kpc^{-1}}$. Grand, Kawata & Cropper (2012) analysing N-body simulations and Monari, Famaey & Siebert (2016), modelling spiral arms with linear perturbation theory, showed that stars located in arms move in towards the Galactic Centre, while stars in interarm regions move outwards. Monari et al. (2016) estimated the gradient in the data to be $\partial V_R / \partial R \simeq -8 \, \mathrm{km \, s^{-1} \, kpc^{-1}}$.

The study by Faure, Siebert & Famaey (2014) of the combined effect of the bar and spiral arms noted that the pattern just described in which stars in arms move inwards reverses outside the corotation resonance, so there stars in arms move outwards while stars between arms move inwards. This finding is consistent with the perturbative model of Monari et al. (2016).

Soon after the gradient in V_R was found in RAVE stars, Widrow et al. (2012) discovered significant deviations in V_z with height z above the plane using the Sloan Digital Sky Survey. Using the high-resolution simulation of Purcell et al. (2011) to study of the effect of the Sagittarius dwarf spheroidal galaxy (dSph) on the MW disc, Gómez et al. (2013) concluded that by plunging through the disc $\sim 2 \, \mathrm{Gyr}$ ago, the Sagittarius dSph could have generated the pattern in V_z detected by Widrow et al. (2012). Carlin et al. (2013) found a similar signature in LAMOST stars that are distributed through a larger volume. Williams et al. (2013) analysed the V_z field defined by RAVE stars, and detected wave-like motions perpendicular to the plane that could either be associated with spiral arms or with a recent accretion event. However, Carrillo et al. (2018), re-analysing the RAVE data, laid bare the extent to which the small measured values of V_z are vulnerable to systematic errors in both proper motions and distances. Using TGAS proper motions and improved distances, they concluded that vertical motions inside the solar radius could be induced by the Galactic bar or spiral arms, while outside they are likely generated by a recent satellite/merging event.

Recently, Antoja et al. (2017) investigated the dependence of the velocity field on metallicity. In a novel analysis applied to data from RAVE and the Geneva–Copenhagen Survey (Holmberg, Nordström & Andersen 2007) they compared the metallicity distribution at (V_R, V_ϕ) with that at $(-V_R, V_\phi)$, which would be identical in a well-mixed axisymmetric model. The fact that the observed metallicity distributions differed is consistent with previous studies (e.g. Famaey et al. 2007) that have shown that the chemical abundances of moving groups differs from that of the local interstellar medium (ISM). In particular, moving groups are not chemically homogeneous, so they cannot be dissolved open clusters.

A significant barrier to uncovering the chemodynamical history of the solar neighbourhood is the difficulty of determining the ages of individual field stars. The classical approach to age determination involves measuring the luminosity of turn-off stars of known colour and metallicity. This method requires an accurate distance. We now have trigonometric parallaxes from the *Tycho–Gaia* Astrometric Solution (TGAS; Gaia Collaboration et al. 2016; Lindegren et al. 2016) for two million stars, so we can determine credible ages for large samples of stars. Here, we combine TGAS parallaxes and proper motions with RAVE spectroscopy of turn-off stars to discover how the velocity field depends on age and metallicity.

In Section 2, we review the RAVE survey and its updated distance pipeline from which our distances and ages are derived (Section 2.2). In Section 2.3, we record the criteria used to select our samples and the steps taken to validate our ages. With our sample of stars in hand, we then explore kinematic trends, in particular $\partial V_{R,\phi} / \partial R$ for two selected age bins (young and old) in Section 3, as a function of Galactocentric radius. Section 4 presents the distributions of orbital parameters for our age-metallicity bins. In Section 5, we present a discussion and interpretation of our results, and draw our conclusions from this analysis.

2 THE DATA

2.1 The RAVE survey

The RAVE survey collected over half a million medium-resolution ($R \approx 7500$) spectra of stars in the Southern hemisphere from 2003 until 2013, using the 6dF multiobject spectrograph on the 1.2-m UK Schmidt Telescope at the Siding Spring Observatory in Australia. Throughout the course of the survey, parameters derived from the spectra were made publicly available via a number of data releases, with the fifth data release (DR5) being the latest (Kunder et al. 2017), providing 520 781 measurements for 457 588 individual stars. Centred on the Ca II-triplet region (8410–8795 Å) region, this spectral range was chosen specifically to coincide with the spectral range of *Gaia*'s Radial Velocity Spectrometer (Prusti 2012; Bailer-Jones et al. 2013; Recio-Blanco et al. 2016).

In addition to radial velocities (typical uncertainties $\sim 2 \, \mathrm{km \, s^{-1}}$; Kordopatis et al. 2013a; Kunder et al. 2017), RAVE DR5 contains a number of other stellar parameters derived from spectra including effective temperature, surface gravity, metallicity ([M/H]), as well as individual abundances for six elements (Mg, Al, Si, Ti, Fe, and Ni) (Boeche et al. 2011). To provide additional parameters such as apparent magnitudes and proper motions, RAVE DR5 was cross-matched with a number of other astrometric and photometric catalogues. In particular, RAVE has a significant overlap with stars available in TGAS (Lindegren et al. 2016), with RAVE DR5 containing 215 590 unique TGAS stars. Currently, the RAVE survey offers one of the largest samples of stars with accurate 6D phase-space information in addition to stellar parameters derived from spectra.

2.2 Distances and ages

We use distances and ages returned by an updated version of the pipeline described in Binney et al. (2014), details of which are given in McMillan et al. (2017). The updated pipeline allows for TGAS parallaxes to be included as priors, alongside stellar parameters such as temperature, surface gravity, and metallicity from RAVE, apparent magnitudes from 2-Micron All-Sky Survey(2MASS; Skrutskie et al. 2006) and AllWISE (Cutri et al. 2013), and an underlying Galactic model. The default Galactic model (prior) used is the same as that used for the distance determinations available in DR4 and DR5 and includes priors on stellar metallicities and ages for a given disc component (McMillan et al. 2017, section 2.1). Details of the other available priors can be found in section 5 of McMillan et al. (2017). From both internal tests and comparisons with external catalogues, McMillan et al. (2017) report that the combined spectrophotometric distance estimates perform better than purely spectroscopic or astrometric estimates.

In addition to distance estimates, the updated pipeline produces estimates of stellar mass, metallicity, line-of-sight extinction, and age as by-products. For this work, we want to avoid a prior where a relationship between age and metallicity is imposed. Therefore, we use age estimates derived utilizing a Galactic model with a flat prior on both age and metallicity ('Density' in McMillan et al. 2017). The ages derived using this prior are roughly consistent with those derived using an age prior where the star formation rate declines over time (McMillan et al. 2017, equation 20), and a flat prior in metallicity. Derived distances are not significantly affected by the choice of prior.

2.3 Age validation

To validate the pipeline's age estimates, we generate a mock catalogue of RAVE-like stars using the population synthesis code GALAXIA (Sharma et al. 2011). As GALAXIA uses PARSEC (Bressan et al. 2012) isochrones to produce stars with perfectly-known ages and atmospheric parameters (T_{eff}, $\log g$, [M/H]), 2MASS photometry, and distances, it offers a suitable test sample for assessing internal uncertainties on the output of the distance pipeline.

2.3.1 Mock catalogue generation

We generated stars with I-magnitude range $7 < I_{\mathrm{DENIS}} < 13$ to cover the whole magnitude range of RAVE, and removed all stars with Galactic latitudes $|b| < 5°$. We then resampled the age distribution of our mock catalogue (primarily by reducing the number of young stars) to ensure we had enough stars for robust statistics across the entire range of stellar ages, and as a side-effect, roughly reproduce the age distribution of the extended solar neighbourhood.

2.3.2 Applying uncertainties to our mock catalogue

We then scattered the mock data for T_{eff}, $\log g$, and [M/H] by RAVE-like uncertainties. The standard deviations used in this process were the quadrature sums of RAVE's internal and external uncertainties for a star with the given true data (for more detail see fig. 5 of Wojno et al. 2017).

The true apparent magnitudes J, H, and K_s in the mock data were then scattered by a Gaussian error distribution with dispersion 0.025 mag, which is a typical 2MASS uncertainty. Finally, the true parallaxes were scattered by a Gaussian error distribution with a

dispersion of 0.3 mas, which is a typical TGAS uncertainty (Gaia Collaboration et al. 2016; Lindegren et al. 2016).

2.3.3 Input versus output age comparison

The mock data were then fed into the updated RAVE distance pipeline and the resulting ages compared with the 'true' ages given by GALAXIA. As a preliminary sanity check the values of T_{eff}, $\log g$, [M/H] and distance from the pipeline were compared with the original values from GALAXIA and found to agree within the errors. Fig. 1 shows the input and output ages subdivided by regions within the $T_{\mathrm{eff}} - \log g$ plane. The top row shows the data for giant stars ($T_{\mathrm{eff}} < 5500$ K, $\log g < 3.5$), the middle row shows the data for main-sequence stars ($\log g > 4.25$), and the bottom row shows the data for turn-off stars (5500 K $< T_{\mathrm{eff}} < 7100$ K, $3.5 < \log g < 4.25$). Panels in the left column are colour-coded by fractional age uncertainty, while panels on the right are colour-coded by absolute age uncertainty. The contours enclose 33, 67, 90, and 99 per cent of the sample. Unsurprisingly, the giant and main-sequence samples have much higher uncertainties than the turn-off sample, with almost all stars being assigned an intermediate age regardless of its true age. Consequently, we exclude all but turn-off stars from further consideration. For turn-off stars, the isochrones are much better separated than for the giant and lower main-sequence stars, and therefore yield smaller age uncertainties (see Fig. 3).

In order to obtain a balanced sample with the most precise age estimates possible, we restrict further analysis to turn-off stars in two age bins: young ($0 < \tau < 3$ Gyr) and old ($8 < \tau < 13$ Gyr) stars. We do not use stars of intermediate age ($3 < \tau < 8$ Gyr) because this age group manifests a significant systematic offset. While this offset disappears if we only consider stars with age uncertainties less than 20 per cent, we find that this prunes the sample in a biased way. Intermediate-age stars are more likely to have large age uncertainties because their errors are unrestricted: a young star cannot have an age smaller than zero, and an old star cannot have an age that exceeds 13.8 Gyr.

2.3.4 Contamination

We now estimate the number of stars that wrongly appear in the 'young' and 'old' bins as a consequence of observational and theoretical uncertainties. In Fig. 2, we show the distributions of input ages of stars that end up in the young ($0 < \tau < 3$ Gyr) and old ($8 < \tau < 13$ Gyr) bins. The dark-shaded areas are regions within which the star has been correctly classified as young or old. The lighter-shaded areas indicate regions in which the star is not as young or old as its bin membership implies, but is nonetheless pretty young ($\tau \leq 4$ Gyr) if it is in the young bin, or pretty old ($\tau \geq 6$ Gyr) if it is in the old bin. From this analysis, we conclude that our 'young' sample has a success rate of ~98 per cent in the sense that less than ~2 per cent of its stars are older than 4 Gyr, and our 'old' sample has a success rate of ~73 per cent in the sense that less than ~27 per cent of its stars are younger than 6 Gyr.

2.4 Selection of our RAVE-TGAS sample

In light of the work presented in the last section, henceforth we confine our analysis to the 37 765 RAVE turn-off stars ($5500 < T_{\mathrm{eff}} < 7100$ K, $3.5 < \log g < 4.25$). This selection in $T_{\mathrm{eff}} - \log g$ space is shown in Fig. 3 by the dashed red lines. Pixels in
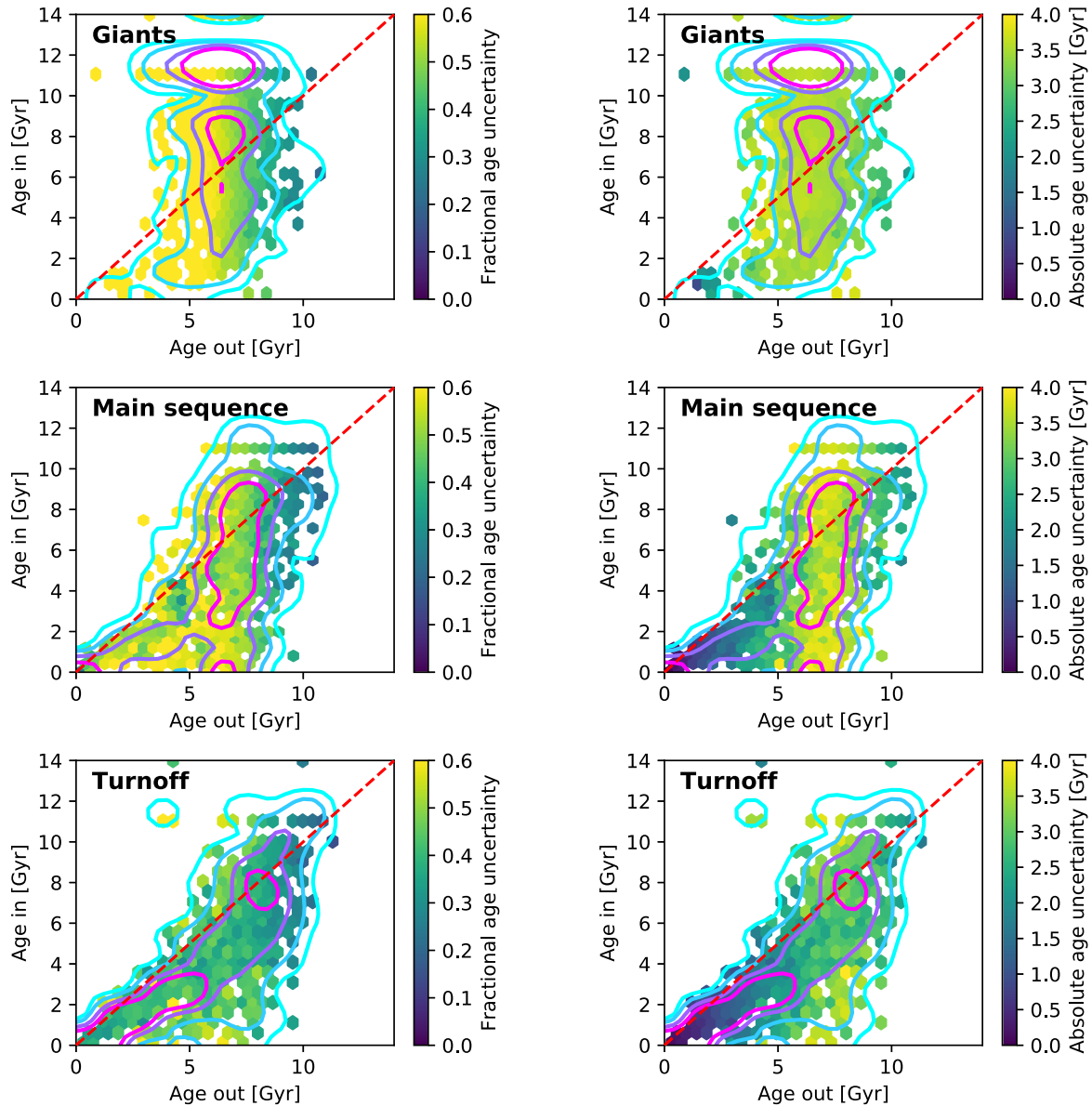
Figure 1. Input age versus output age, with bins coloured by fractional age uncertainty in the left column, and by absolute age uncertainty in the right column. Giants ($T_{eff} < 5500$ K, $\log g < 3.5$), main-sequence stars ($\log g > 4.25$), and turn-off stars ($T_{eff} > 5500$ K, $3.5 < \log g < 4.25$) are shown as the top, middle, and bottom rows, respectively. Contours indicate 33, 67, 90, and 99 per cent of the sample.

Fig. 3 are colour-coded by fractional age uncertainty, with solar-metallicity isochrones overplotted in black, spanning a range in age from 1 to 13 Gyr in steps of 1 Gyr.

A histogram of the age uncertainties for this sample is shown in Fig. 4. The majority of our sample (∼60 per cent) has age uncertainties less than 2 Gyr, with a sizable fraction (∼25 per cent) having age uncertainties less than 1 Gyr.

2.4.1 RAVE quality criteria

We further restrict analysis to stars that have a high signal-to-noise ratio (SNR_K); a reasonable estimate for their line-of-sight velocity (eHRV); reliable atmospheric parameters because (i) the stellar-parameter pipeline converged (Algo_Conv_K; Kordopatis et al. 2013a) and (ii) the fit between the best-fitting model and the observed spectrum from the chemical pipeline (CHISQ_c; Boeche

et al. 2011) was reasonable. In addition, we remove peculiar stars flagged by the classification pipeline as having anomalous spectra (Matijevič et al. 2012). Quantitatively, we require

(i) SNR_K > 40
(ii) eHRV < 8 km s^{-1}
(iii) Algo_Conv_K $\neq$ 1
(iv) CHISQ_c < 2000
(v) c1 = d, g, h, n, or o
(vi) c2 = d, g, h, n, o, or e
(vii) c3 = d, g, h, n, o, or e

We then apply the age bins described in Section 2.3.3: young ($0 < \tau < 3$ Gyr) and old ($8 < \tau < 13$ Gyr), to this sample of turn-off stars. After applying these criteria, we are left with 6630 'young' stars and 5072 'old' stars. The spatial distributions of our selected
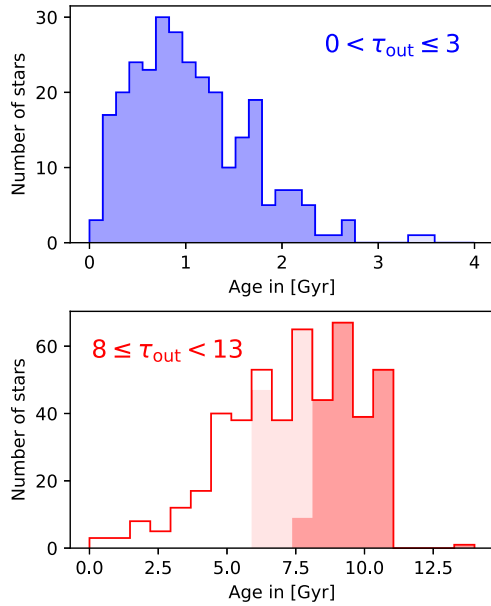
Figure 2. Distribution of input ages for the stars with output ages given by the range indicated in the plot. The top panel shows the distribution for our 'young' sample, while the bottom panel shows the distribution for our 'old' sample. The darker shaded regions indicate stars with input ages that fall within the given bin, while the lighter shaded regions indicate stars with input ages that fall slightly outside of the given bin. A lack of shading indicates stars which are considered contaminants of that bin.
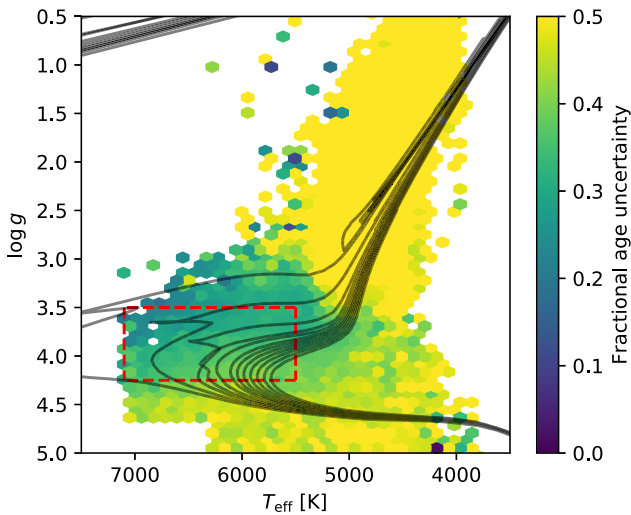
Figure 3. Spectroscopic $T_{eff} - \log g$ diagram of RAVE DR5 stars which satisfy the quality criteria listed in Section 2.4.1. The dashed red lines indicate the cuts made in the parameter space to select for only turn-off stars. The bins are colour-coded by the fractional age uncertainty. Solar-metallicity isochrones are overplotted in black, and span a range in age from 1 to 13 Gyr, with a step size of ~1 Gyr.

young and old populations are shown in Fig. 5 with blue and red contours, respectively.

2.4.2 Metallicity bins

We divide each age group into the four metallicity bins illustrated in Fig. 6. The bins are:
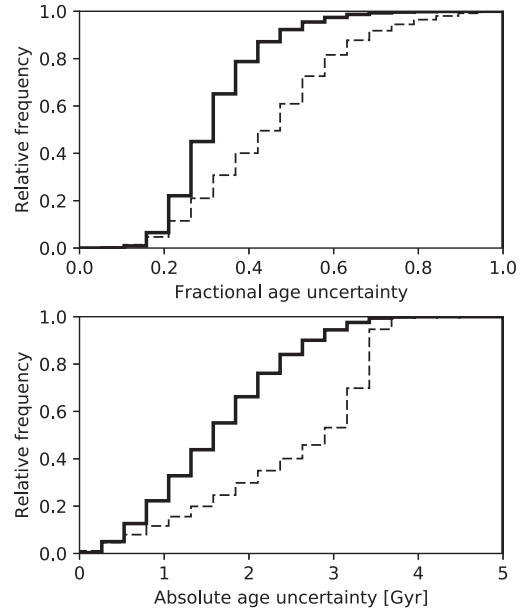

Figure 4. Cumulative histogram of the fractional (top) and absolute (bottom) age uncertainties of our final selected sample of turn-off stars (solid line), and for the whole RAVE-TGAS sample (dashed line).
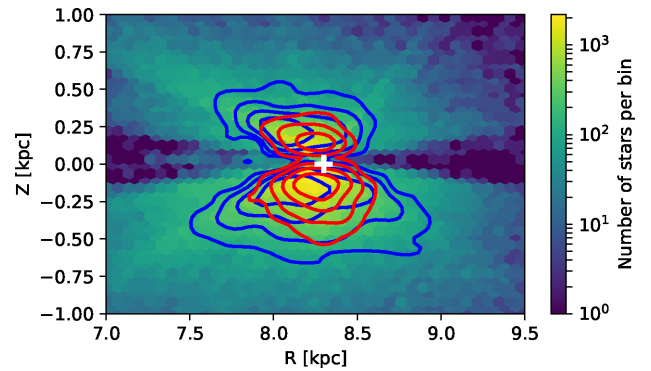

Figure 5. Spatial extent of the selected young (blue contours) and old (red contours) turn-off stars. Contours indicate 33, 67, 90, and 99 per cent of each sample. The spatial extent and density of the entire RAVE-TGAS sample (i.e. all spectral types) is shown by the 2D histogram beneath. The white plus indicates the position of the Sun.
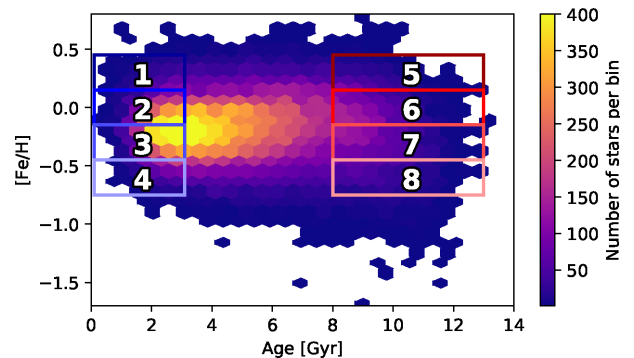

Figure 6. Age versus [Fe/H] 2D histogram for our sample of turn-off stars defined by the red dashed lines in Fig. 3, colour-coded by density. We consider four metallicity bins for each age group, described in Section 2.4.2.

(i) Bins 1 and 5: $0.15 \leq$ [Fe/H] < 0.45
(ii) Bins 2 and 6: $-0.15 \leq$ [Fe/H] < 0.15
(iii) Bins 3 and 7: $-0.45 \leq$ [Fe/H] < -0.15
(iv) Bins 4 and 8: $-0.75 \leq$ [Fe/H] < -0.45

Throughout the rest of the text, we will refer to these bins by the numbers listed above and shown in Fig. 6. We note that the radial distribution of stars does not vary significantly between these metallicity bins, for both the young (Bins 1–4) and old (Bins 5–8) samples. Our young sample has a Galactocentric radial distribution that peaks at $R \sim 8.2$ kpc, with $\sigma_R \sim 0.25$ kpc, and for old stars, $R \sim 8.25$ kpc and $\sigma_R \sim 0.12$ kpc (see Fig. 5).

3 VELOCITY DISTRIBUTIONS

We now examine for each of the eight age–metallicity bins marked in Fig. 6 the distributions of V_R, V_ϕ, and V_z. We determine Galactocentric velocities in cylindrical coordinates following appendix A of Williams et al. (2013) with the location of the Sun taken to be $(R_0, z_0) = (8.3, 0)$ kpc, and the local circular speed to be $V_{LSR} = 240$ km s^{-1} (Schönrich 2012), and the solar peculiar velocity to be $(U, V, W)_\odot = (11.10, 12.24, 7.25)$ km s^{-1} (Schönrich, Binney & Dehnen 2010). V_R is positive for motion away from the Galactic Centre, V_ϕ is positive in the direction of Galactic rotation, and V_z is positive towards the north Galactic pole. Line-of-sight velocities are provided by RAVE DR5 (Kunder et al. 2017), and proper motions are taken from the TGAS catalogue (Lindegren et al. 2016).

3.1 Correcting by the selection function of RAVE

As RAVE is not a volume-complete survey, when computing kinematic trends we need to correct for the selection function. Wojno et al. (2017) and references therein show that the selection function of RAVE is relatively simple and well-behaved in the sense that RAVE is not kinematically or chemically biased wherever its stellar parameter pipeline gives reliable results. However, our sample comprises exclusively stars contained in both RAVE and TGAS, which had vastly different observing strategies and sky completeness, and therefore we had to reevaluate the selection function S_{select}. We computed S_{select} as a function of position on the sky in HEALPIX (Górski et al. 2005) pixels, I_{2MASS} magnitude, and $(J - K_s)$ colour from the definition

$$S_{select}(pixel_{\alpha,\delta}) = \frac{\sum \sum N_{RAVE}(pixel_{\alpha,\delta}, I, J - K_s)}{\sum \sum N_{2MASS}(pixel_{\alpha,\delta}, I, J - K_s)}. \quad (1)$$

Each star contributes to the statistical analysis with a weight $w_i = 1/S_{select}$ in the sense that the weighted mean $\overline{x}$ and weighted dispersion σ_x of an observable x are

$$\overline{x} = \frac{\sum_{i=1}^{n}(x_i \times w_i)}{\sum_{i=1}^{n} w_i}, \quad (2)$$

$$\sigma_x^2 = \frac{\sum_{i=1}^{n} w_i(x_i - \overline{x})^2}{k \sum_{i=1}^{n} w_i}, \quad (3)$$

where $k = (N' - 1)/N'$, and N' is the number of non-zero weights.

3.2 Velocity trends with age and [Fe/H]

Fig. 7 shows (left to right) the weighted distributions of V_R, V_ϕ, and

V_z for stars in the young bin (blue, top row), and the old bin (red, bottom row), with each age bin divided into the four metallicity bins defined in Fig. 6. Statistics for each histogram, computed according to equations (2) and (3), are given in Table 1. We note that the values of $\sigma_{R,\phi,z}$ given in Table 1 have been corrected for the contribution of observational uncertainties:

$$\sigma_{R,\phi,z} = \sqrt{\sigma_{R,\phi,z}^2 - e_{V_{R,\phi,z}}^2} \quad (4)$$

where $e_{V_{R,\phi,z}}$ is the reported uncertainty for each component of the velocity, weighted by the selection function.

The values in Table 1 for young stars (upper block) show that V_R and V_z do not vary significantly with metallicity. By contrast, V_ϕ increases as [Fe/H] decreases. An inverse correlation of V_ϕ with [Fe/H] within the thin disc is well known (e.g. Lee et al. 2011; Adibekyan et al. 2013; Recio-Blanco et al. 2014; Wojno et al. 2016; Kordopatis et al. 2017), and recognized to be a signature of the metallicity gradient within the thin disc (e.g. Schönrich et al. 2010): metal-poor stars tend to have large guiding-centre radii and to visit us near pericentre, whereas metal-rich stars tend to have small guiding-centre radii and visit us near apocentre. Quantitatively, we find

$$\frac{\partial V_\phi}{\partial [Fe/H]} \approx -15 \, \text{km s}^{-1} \, \text{dex}^{-1} \quad \text{(young stars)}. \quad (5)$$

We estimate this value by a simple linear fit to the values of $\overline{V_\phi}$ for the four metallicity bins, taking the centre of the metallicity bin for the value on the x-axis. Previous estimates of $\partial V_\phi / \partial [Fe/H]$ have ranged from -23 to -11 km s^{-1} dex^{-1}. While our estimate is comparable, literature values usually indicate a steeper gradient than we find.

Table 1 indicates that σ_ϕ decreases as metallicity decreases, with Bin 1 having a dispersion $\sigma_\phi = 23.6 \pm 0.8$ km s^{-1} and Bin 4 having $\sigma_\phi = 18.0 \pm 0.5$ km s^{-1}. This trend is a natural corollary of an increase in mean Galactocentric radius with decreasing metallicity and the stellar disc becoming cooler as one moves outward. The data for σ_R suggest, however, that we treat the trend in σ_ϕ with caution because they do not show a corresponding decrease while dynamical theory requires σ_R and σ_ϕ to vary together.

In line with much previous work (e.g. Nordström et al. 2004; Guiglion et al. 2015) the histograms for old stars are broader than those for young stars. All three velocity dispersions increase with decreasing [Fe/H], so amongst old stars the metal-poor component is the hottest – this is the reverse of the trend in σ_ϕ that we just saw in the young stars. Gratifyingly, the data for V_ϕ for old stars show it to decrease as [Fe/H] increases, just as dynamical theory requires given the increase in σ_ϕ. Many previous studies (e.g. Spagna et al. 2010; Kordopatis et al. 2011; Adibekyan et al. 2013; Kordopatis et al. 2013b; Wojno et al. 2016; Kordopatis et al. 2017) have found the same trend of V_ϕ with [Fe/H], but they have generally obtained a steeper gradient than our value

$$\frac{\partial V_\phi}{\partial [Fe/H]} \approx 5 \, \text{km s}^{-1} \, \text{dex}^{-1} \quad \text{(old stars)}. \quad (6)$$

Measurements from the literature range from 42 to 51 km s^{-1} dex^{-1}. The literature values are much larger than ours, probably because they refer to samples of thick disc stars (selected chemically, kinematically, or spatially), whereas we have imposed no such selection.

Fig. 8 shows the distribution of young (blue) and old (red) stars in the $(-V_R, V_\phi)$ plane, which is the natural extension of the traditional (U, V) plane. The histograms in the left and central columns of Fig. 7 are projections of these distributions on to the V_R and V_ϕ axes. In Fig. 8, metallicity increases from left to right. Literature values for
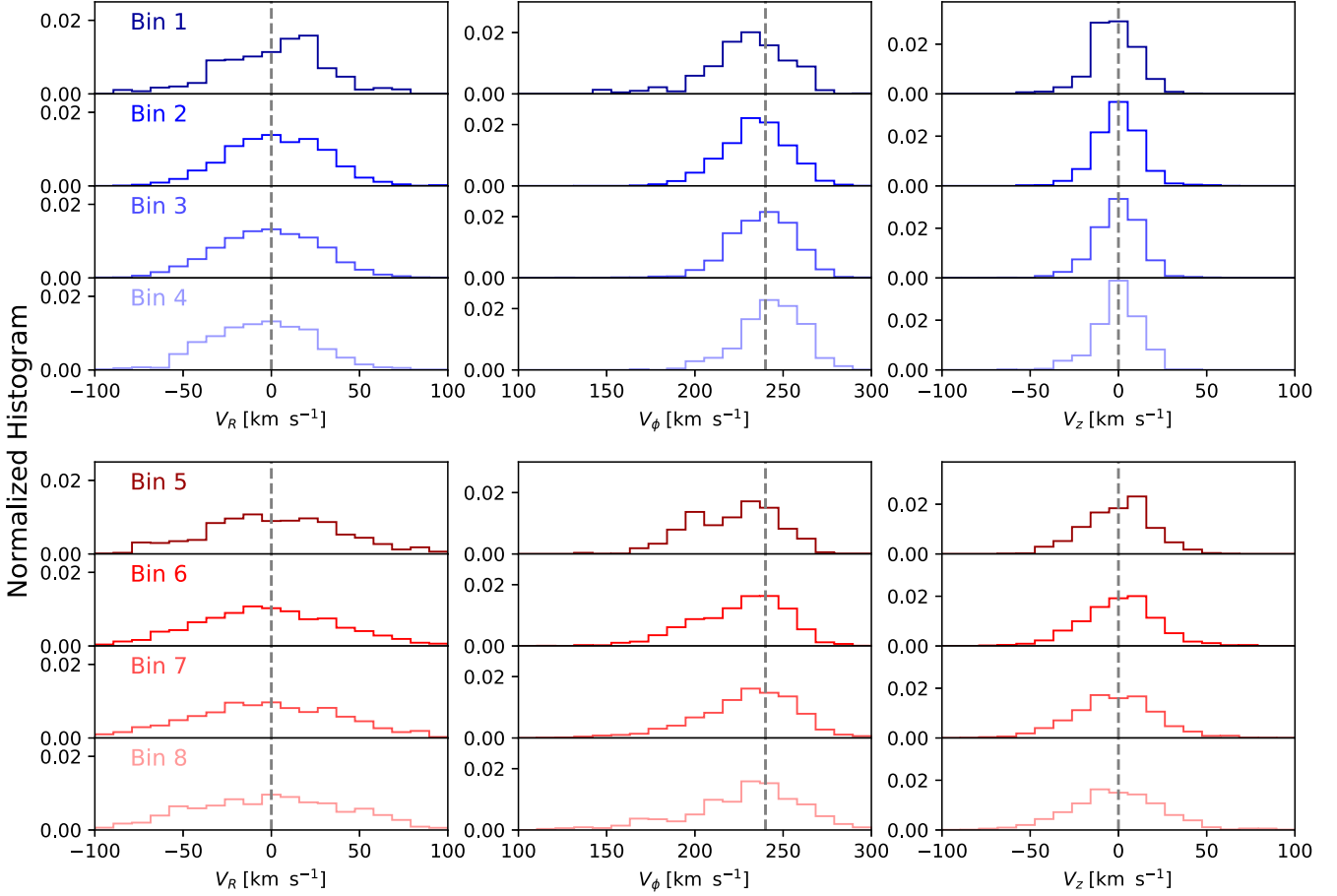
Figure 7. Cylindrical velocity distributions (left to right: V_R, V_ϕ, V_z), weighted by the selection function, for our two age bins. Young stars are plotted in blue, old stars are plotted in red. More metal-rich bins are plotted with darker colours, with more metal-poor bins in lighter colours (metallicity Bins 1, 2, 3, and 4 for young stars, and Bins 5, 6, 7, and 8 for old stars). Grey dashed lines indicate 0 km s^{-1} for the V_R and V_z components, and 240 km s^{-1} for the V_ϕ component.

Table 1. Mean and dispersion for each component of the Galactocentric cylindrical velocity, weighted by the selection function, for both age groups and each metallicity bin within the age groups.

Bin number	Metallicity range	N	$\overline{V_R}$	σ_R	$\overline{V_\phi}$	σ_ϕ	$\overline{V_z}$	σ_z
Young								
1	$0.15 \leq [Fe/H] < 0.45$	386	0.5 ± 1.3	30.3 ± 1.1	229.3 ± 1.0	23.6 ± 0.8	-2.4 ± 0.5	12.8 ± 0.5
2	$-0.15 \leq [Fe/H] < 0.15$	2534	2.1 ± 0.4	27.2 ± 0.4	234.0 ± 0.3	18.4 ± 0.3	-0.2 ± 0.2	12.9 ± 0.2
3	$-0.45 \leq [Fe/H] < -0.15$	3141	-1.8 ± 0.4	30.1 ± 0.4	237.7 ± 0.3	18.6 ± 0.2	-0.3 ± 0.2	13.2 ± 0.2
4	$-0.75 \leq [Fe/H] < -0.45$	542	-5.6 ± 1.0	29.2 ± 0.9	243.2 ± 0.6	18.0 ± 0.5	0.1 ± 0.5	12.6 ± 0.4
Old								
5	$0.15 \leq [Fe/H] < 0.45$	531	0.4 ± 1.4	39.3 ± 0.6	222.1 ± 0.9	24.4 ± 0.9	0.1 ± 0.7	19.0 ± 1.2
6	$-0.15 \leq [Fe/H] < 0.15$	1757	-2.2 ± 0.8	40.5 ± 1.0	225.6 ± 0.5	25.8 ± 1.6	0.5 ± 0.4	21.2 ± 2.0
7	$-0.45 \leq [Fe/H] < -0.15$	1740	-2.6 ± 0.8	43.2 ± 1.0	228.7 ± 0.6	28.9 ± 1.4	-2.2 ± 0.5	24.3 ± 1.7
8	$-0.75 \leq [Fe/H] < -0.45$	838	-2.5 ± 1.3	47.2 ± 0.6	227.5 ± 0.9	32.9 ± 0.9	-1.6 ± 0.8	27.3 ± 1.0

local maxima associated with the Hercules (cyan cross), Hyades (magenta square), and Pleiades (green triangle) moving groups are overplotted (Dehnen 2000; Binney & Tremaine 2008).

The peak in the distribution of young stars moves up and to the right with decreasing metallicity, as we expect given that for these stars $\partial V_\phi/\partial [Fe/H] < 0$ and $\partial V_R/\partial [Fe/H] > 0$. With the possible exception of the Hercules stream (cyan cross) the contours do not provide convincing evidence for the streams detected by Dehnen (2000) in Hipparcos data. Curiously, the signature of the Hyades stream is most convincing for the most metal-poor Bins 4 and 8.

Given the small size of the sample of old stars, and the way the red contours change from one metallicity panel to another, we conclude that these wiggles probably owe more to noise than moving groups.

The histograms for V_z in the right column of Fig. 7 show that, as expected, the old stars are vertically hotter than the young stars. Whereas for the old stars σ_z tends to increase with decreasing metallicity, from $\sigma_z = 19.0 \pm 1.2$ km s^{-1} for Bin 5 to $\sigma_z = 27.3 \pm 1.0$ km s^{-1} for Bin 8, σ_z is essentially independent of metallicity for the young stars. The increase for old stars in σ_z with
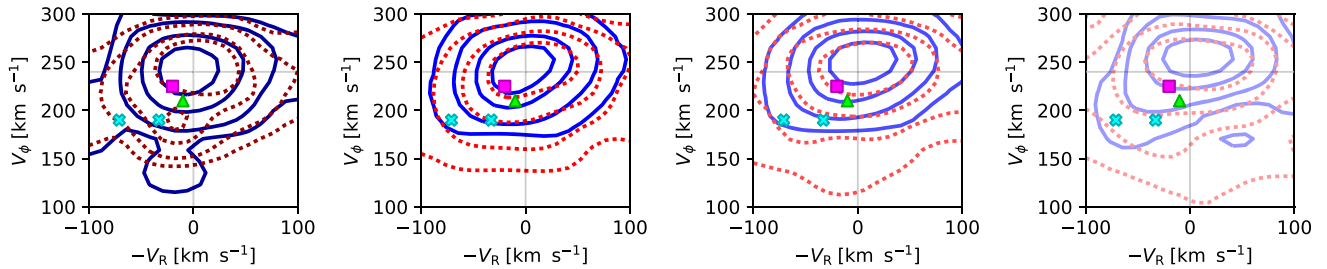
Figure 8. $-V_R$ and V_ϕ space for our sample of young (blue, solid) stars and old (red, dashed) stars splits into the four metallicity bins shown in Fig. 6. Contours show the density distributions for 33, 67, 90, and 99 per cent of the sample for each bin. The most metal-rich bin ($0.15 \leq$ [Fe/H] < 0.45) is on the left, and the most metal-poor bin ($-0.75 \leq$ [Fe/H] < -0.45) is on the right. Cyan crosses indicate the two peaks in the kinematics of the Hercules moving group. The Hyades and Pleiades moving groups are indicated with a magenta square and a green triangle, respectively.
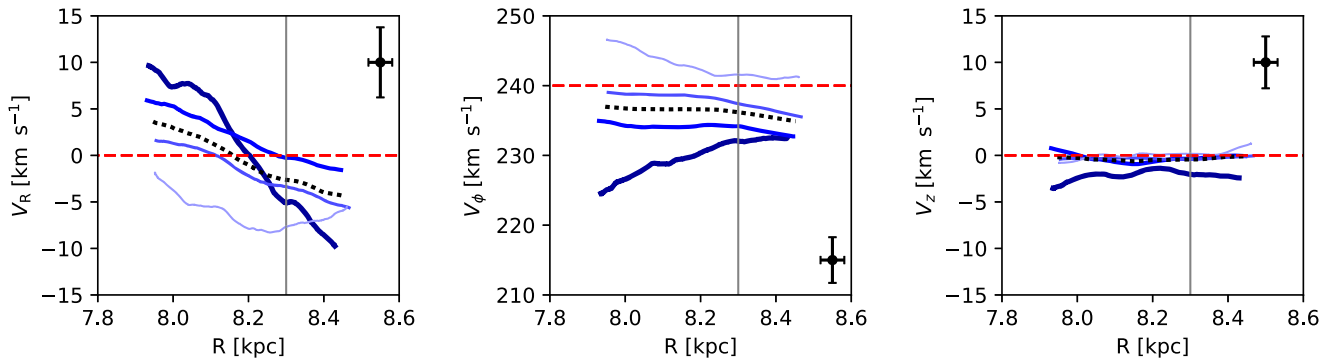
Figure 9. Velocity trends as a function of Galactocentric radius (left to right: V_R, V_ϕ, V_z), weighted by the selection function, for our young stars. The trend for the entire young sample ($-0.75 \leq$ [Fe/H] < 0.45) is indicated with the black dotted line. The most metal-rich bin ($0.15 \leq$ [Fe/H] < 0.45) is indicated with the thick, dark blue line, and the most metal-poor bin ($-0.75 \leq$ [Fe/H] < -0.45) with the thin, light blue line. The solid grey line indicates the position of the Sun. Average uncertainties are indicated in each panel by the error bar.
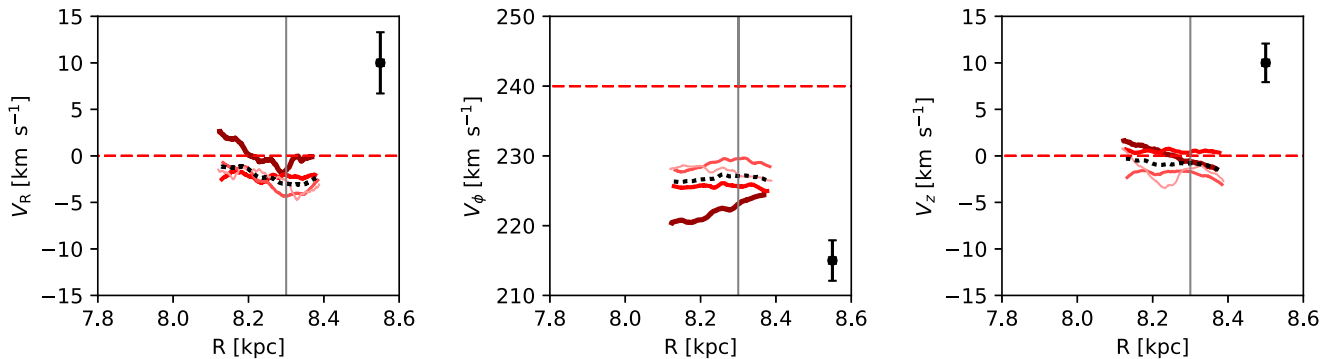

Figure 10. Velocity trends as a function of Galactocentric radius (left to right: V_R, V_ϕ, V_z), weighted by the selection function, for our old stars. The trend for the entire old sample ($-0.75 \leq$ [Fe/H] < 0.45) is indicated with the black dotted line. The most metal-rich bin ($0.15 \leq$ [Fe/H] < 0.45) is indicated with the thick, dark red line, and the most metal-poor bin ($-0.75 \leq$ [Fe/H] < -0.45) with the thin, light pink line. The solid grey line indicates the position of the Sun. Average uncertainties are indicated in each panel by the error bar.

decreasing [Fe/H], like the decrease in V_ϕ with decreasing [Fe/H], points to old, metal-poor stars being on highly eccentric orbits that are not tightly confined to the plane.

3.3 Velocity trends with R

We now consider kinematic trends with Galactocentric radius. In Figs 9 and 10, we show V_R, V_ϕ, V_z as functions of R for the young and old stars, respectively. Metal-rich bins are shown in darker colours with thicker lines, with successively lighter colours and

thinner lines indicating decreasing metallicity. The plotted values are calculated as follows. The stars in a given age–metallicity bin were ordered by R and then a window containing N stars was moved along the resulting lineup, and the mean of V_R, etc., was computed at each location of the window. This operation was carried out for 1000 values of N that were drawn from a uniform distribution with a minimum of 20, and a maximum which varied as a function of the size of the age–metallicity bin. The results were then averaged. Average uncertainties for each velocity component are given in their respective panels. The uncertainty in R largely correlates with

Table 2. Measured radial velocity gradients for each age group and metallicity bin.

Bin number	Metallicity range	$\partial V_R/\partial R$ (km s^{-1} kpc^{-1})
Young		
1	$0.15 \leq$ [Fe/H] < 0.45	-28.0 ± 9.9
2	$-0.15 \leq$ [Fe/H] < 0.15	-10.6 ± 3.8
3	$-0.45 \leq$ [Fe/H] < -0.15	-10.2 ± 3.6
4	$-0.75 \leq$ [Fe/H] < -0.45	-3.6 ± 1.3
All	$-0.75 \leq$ [Fe/H] < 0.45	-11.4 ± 4.0
Old		
5	$0.15 \leq$ [Fe/H] < 0.45	-5.9 ± 2.5
6	$-0.15 \leq$ [Fe/H] < 0.15	-0.7 ± 1.1
7	$-0.45 \leq$ [Fe/H] < -0.15	-9.9 ± 4.2
8	$-0.75 \leq$ [Fe/H] < -0.45	-6.8 ± 2.8
All	$-0.75 \leq$ [Fe/H] < 0.45	-5.9 ± 2.6

the range in Galactocentric radius sampled, and is of the order of ~ 0.03 and ~ 0.01 kpc for young and old stars, respectively. Measurements of $\partial V_R/\partial R$ for each age-metallicity bin are given in Table 2.

To check that this procedure generates velocity gradients that are consistent with published gradients, we used it to compute velocity gradients for (i) the complete set of turn-off stars, i.e. all stars in the red dashed rectangle of Fig. 3, regardless of age or metallicity, and (ii) the set of red giant stars ($2 < \log g < 2.5$) that satisfy the quality criteria given in Section 2.4.1. For the turn-off stars, we find $\partial V_R/\partial R = -5.7 \pm 2.0$ km s^{-1} kpc^{-1}, while for the giant stars, $\partial V_R/\partial R = -5.4 \pm 2.1$ km s^{-1} kpc^{-1}. Both of these values agree well with literature values: -3 km s^{-1} kpc^{-1} from Siebert et al. (2011), -8 km s^{-1} kpc^{-1} from Williams et al. (2013), and -6.6 ± 0.7 km s^{-1} kpc^{-1} from Bovy (2017). Negative values of $\partial V_R/\partial R$ signal that we lie in a region in which the stellar fluid is being compressed as stars at both smaller and larger radii are moving towards us.

3.3.1 Young stars ($0 < \tau < 3$ Gyr)

The dashed black lines in Fig. 9 show the velocity trends for our entire sample of young stars, summed over all four metallicity bins. The gradient of the curve in the panel for V_R is $\partial V_R/\partial R = -11.4 \pm 4.0$ km s^{-1} kpc. When the sample is decomposed by metallicity, the gradient $\partial V_R/\partial R$ of the most metal-rich bin (1) is markedly steeper (-28.0 ± 9.9 km s^{-1} kpc^{-1}) than those of Bins 2 and 3. The curve $V_R(R)$ for the most metal-poor bin (4) shifts from a negative gradient at smaller radii to a positive gradient at the largest values of R. The gradients we obtain for Bins 1, 2, and 3 are all steeper than typical literature values for more inhomogeneous populations ($\lesssim -3$ km s^{-1} kpc from Siebert et al. (2011); -8 km s^{-1} kpc^{-1} from Williams et al. (2013); -6.6 ± 0.7 km s^{-1} kpc^{-1} from Bovy (2017); -7.01 ± 0.61 km s^{-1} kpc^{-1}, and -9.42 ± 1.77 km s^{-1} kpc^{-1} from Carrillo et al. (2018) for measurements made below and above the plane of the disc, respectively).

The central panel of Fig. 9 displays again the familiar result that at any radius V_ϕ decreases with increasing [Fe/H] (the upper central panel of Fig. 7). The new result we take from Fig. 9 is that the sign of $\partial V_\phi/\partial R$ changes from positive for the metal-rich Bin 1 to negative for the metal-poor Bin 4. This trend amongst our young stars is consistent with a finding of Rojas-Arriagada et al. (2016, their fig. 8) for the thin disc as a whole.
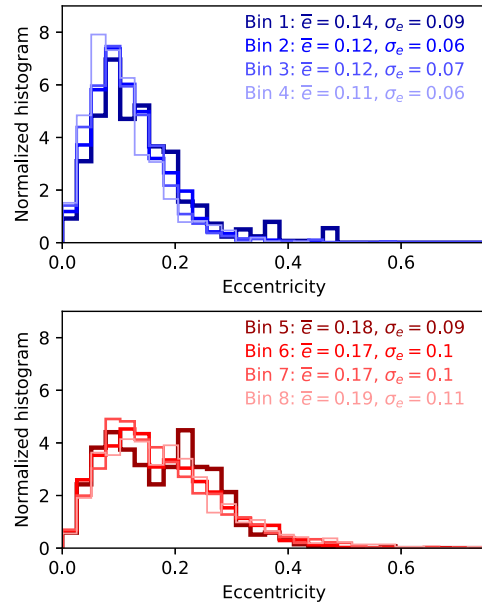
Figure 11. Orbital eccentricities for our sample of young (top) and old (bottom) stars. Bins in metallicity are defined in Section 2.4.2.

The right-hand panel of Fig. 9 shows that V_z is consistent with zero at all radii for all metallicity bins.

3.3.2 Old stars ($8 < \tau < 13$ Gyr)

Fig. 10 shows the dependence of V on R for old stars. Unfortunately, the old stars probe a significantly smaller range in R than do the young stars.

When all four metallicity bins are aggregated, we obtain a negative gradient, $\partial V_R/\partial R = -5.9 \pm 2.6$ km s^{-1} kpc^{-1}. There is a suggestion that the mean value of V_R decreases with decreasing metallicity, but there is no evident variation of $\partial V_R/\partial R$ with metallicity, contrary to what we found for the young stars.

All four metallicity bins of old stars have lagging values of $V_\phi \sim -14$ km s^{-1}, as we expect given the relatively large velocity dispersions of these populations. Any dependence on metallicity of the gradient $\partial V_\phi/\partial R$ is, for the most part, lost in the noise, contrary to what we found for the young stars. However, we do find that the most metal-rich bin (5) has the greatest lag, similar to Bin 1 for young stars.

The old stars, like the young stars, show no systematic dependence of V_z on either metallicity or radius, and for all populations V_z is consistent with zero.

4 ORBITAL PARAMETERS

An orbit in the MWPotential2014 potential was computed for each star using the GALPY (Bovy 2015) PYTHON package. From the orbit, we tabulated the eccentricity e, guiding radius (R_G), and the maximum height above the plane $z_{\max}$.

4.1 Eccentricities

In Fig. 11, we show the eccentricity distributions for our young (left-hand panel) and old stars (right-hand panel), divided into bins of metallicity and weighted by the factors w_i defined in Section 3.1.
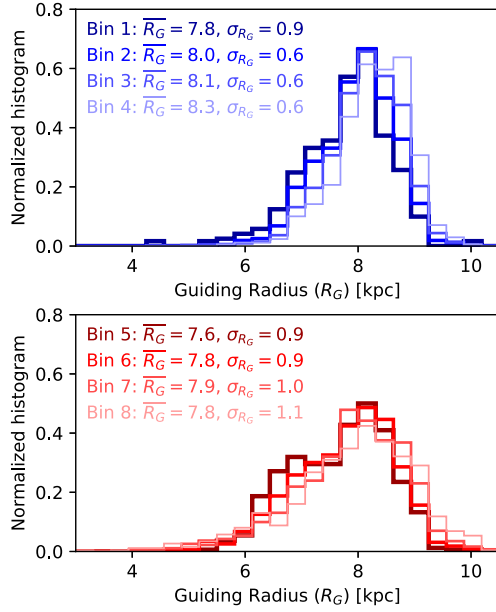
Figure 12. Maximum height above the plane (Z_{max}) for our sample of young (top) and old (bottom) stars. Bins in metallicity are defined in Section 2.4.2.
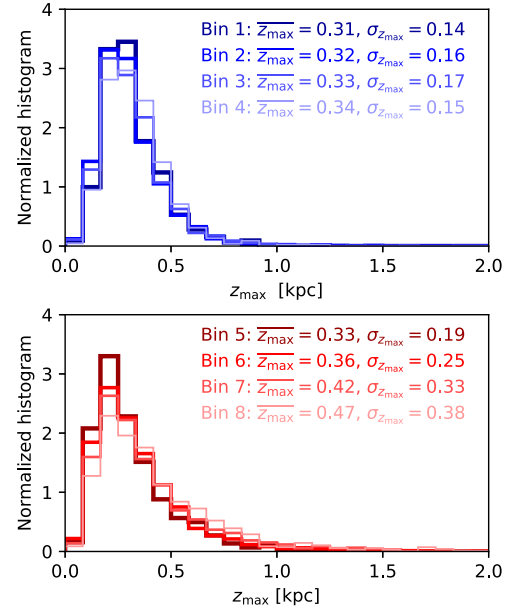

Figure 13. Maximum height above the plane (Z_{max}) for our sample of young (top) and old (bottom) stars. Bins in metallicity are defined in Section 2.4.2.

When all four metallicity bins are aggregated, the eccentricity distribution of our young stars peaks at $\overline{e} = 0.12$ and has dispersion $\sigma_e = 0.07$ (typical of the thin disc). The mean value of e shifts to smaller values with decreasing metallicity ($\overline{e} = 0.14$ for Bin 1 and $\overline{e} = 0.11$ for Bin 4), and the dispersion of e decreases slightly with decreasing metallicity.

The old stars have a much broader distribution in e, and consequently a larger mean eccentricity. When the metallicity bins are aggregated, the mean eccentricity of old stars is $\overline{e} = 0.18$ and its dispersion is $\sigma_e = 0.1$ (typical of the thick disc, see Kordopatis et al. 2011). In contrast to the young population, the mean and dispersion of the eccentricity distributions are very similar, and slightly increase with decreasing metallicity: the mean e increases from $\overline{e} = 0.18$ for Bin 5 to $\overline{e} = 0.19$ for Bin 8. We note that for the most metal-rich bin ($0.15 \leq$ [Fe/H] < 0.45), the histogram is suggestive of a bimodality in the eccentricity distribution. Uncertainties in $\overline{e}$ and σ_e are of the order ~ 0.01.

4.2 Guiding radii

The distributions of guiding radii for our young and old samples are shown in Fig. 12. Young stars have mean guiding radii closer to the solar neighbourhood ($\overline{R_G} = 7.8 - 8.3$ kpc) compared to old stars, which have guiding radii towards the inner disc ($\overline{R_G} = 7.6 - 7.9$ kpc). The dispersion in guiding radii is also larger for old stars. We also note a hint of a bimodality in the guiding radii distribution for old, metal-rich stars, similar to their eccentricity distribution. In addition, for young stars, we find an increase in guiding radii as a function of decreasing metallicity, corresponding to the results shown in Fig. 11. Uncertainties in $\overline{R_G}$ and σ_{R_G} are of the order ~ 0.03 kpc.

4.3 Maximum height above the plane

In Fig. 13, we show the distributions of z_{max} for our young and old stars. All metallicity bins of young stars have similar means ($\overline{z_{max}} = 0.31 - 0.34$ kpc). For young stars, uncertainties on $\overline{z_{max}}$

and $\sigma_{z_{max}}$ are of the order ~ 0.01 kpc. By contrast the old stars show a significant difference in mean Z_{max} between the most metal-rich (Bin 5, $\overline{z_{max}} = 0.3$ kpc), and the most metal-poor bin ($\overline{z_{max}} = 0.52$ kpc). Uncertainties on $\overline{z_{max}}$ and $\sigma_{z_{max}}$ for old stars are of the order ~ 0.02 kpc.

The distributions of z_{max} for young and old stars are remarkably similar. Both are very skew, but the distribution for old stars has a much stronger tail towards high z_{max}. In interpreting these distributions of z_{max}, it must be borne in mind that RAVE's sightlines avoid the plane, so stars tend to be observed at significant values of z. Clearly, $z_{max} \geq z$. Given the strong correlation of σ_z with age established in earlier work (e.g. Casagrande et al. 2011), most of the youngest stars in the disc have no chance of entering the RAVE catalogue because they do not move far enough from the plane. That is, RAVE must be catching only the high-V_z tail of the youngest stars.

5 DISCUSSION AND CONCLUSIONS

The release of *Gaia*-based parallaxes for the majority of RAVE stars has significantly enhanced the value of the RAVE catalogue by reducing errors in distances and proper motions, particularly for main-sequence and turn-off stars. The new parallaxes also make it possible to determine credible ages for stars in the turn-off region. It is well established that the kinematics of a stellar population is correlated with age and chemistry. Since these correlations arise from the secular evolution of the Galaxy's mass distribution, star-formation rate, and non-axisymmetric features (e.g. Aumer, Binney & Schönrich 2016; Schönrich & McMillan 2017), they must encode valuable information about our Galaxy's history. Hence, it is interesting to re-examine the kinematics–age–metallicity nexus for turn-off stars that appear in both the RAVE and TGAS catalogues.

Unfortunately, even for stars in the RAVE-TGAS overlap, ages are quite uncertain, so we have restricted the analysis to the youngest ($\tau < 3$ Gyr) and oldest ($\tau > 8$ Gyr) stars in the expectation that the given uncertainties cannot scatter stars from one extreme group to the other. A corollary of this restriction is that the studied samples are

rather small: 6630 young stars and 5072 old stars. We note that while we expect our young stars to be relatively free of contamination, the same cannot be said for the old stars, where we estimate $\sim$27 per cent have true ages less than 6 Gyr.

A feature of samples drawn from RAVE that one must always bear in mind is that few RAVE stars lie close to the plane, and distance from the Sun and distance from the plane are correlated. These features arise because RAVE avoids sightlines at low Galactic latitudes. A significant corollary for our sample of young stars is that they must all be outliers in the true distribution of vertical energy and they may not be typical of young stars as a whole.

While the young stars cover a range of $\sim$0.5 kpc in R, the sample of old, less luminous stars, has not much more than half the radial range. Consequently, it is hard to establish radial trends for the old stars.

We have used hot turn-off stars to conduct our analysis, and here, we note a small caveat regarding RAVE turn-off stars and their derived distances. Kunder et al. (2017) found that distances to RAVE's hot dwarfs in DR5 were some of the most problematic, and an erroneous distance can result in motion associated with differential rotation artificially enhancing values derived for V_R (Schönrich, Binney & Asplund 2012). However, McMillan et al. (2017), using TGAS parallaxes as a prior to provide updated distance measurements, found that systematic uncertainties were greatly reduced for turn-off stars (see their section 7). Therefore, while we cannot be completely sure that these results are not artefacts induced by systematic errors in the distances to these hot turn-off stars, we have little reason to believe that our results are simply due to systematics.

Overall, we find negative radial velocity gradients as a function of Galactocentric radii and measure steeper gradients than those found before for RAVE stars (Siebert et al. 2011; Williams et al. 2013). The source of the negative gradient in $\partial V_R/\partial R$ is typically attributed to flows induced by non-axisymmetries in the disc (i.e. the bar and/or spiral arms, Siebert et al. 2011, 2012). When we split each age group into bins of metallicity, we show, for the first time, that $\partial V_R/\partial R$ steepens with metallicity. While a signature of this trend is found in both the young and old stars, it is much more pronounced for young stars.

A possible physical interpretation for this difference may be found by revisiting the $-V_R$; V_ϕ plane (Fig. 8, analogous to the U; V plane). We recall that moving groups in the local velocity field have been associated with the effects of resonant gravitational interactions due to non-axisymmetries in the MW disc, e.g. the Hercules moving group is typically explained as a signature of a bar that perturbs the orbits of stars near its OLR (e.g. Dehnen 2000; Fux 2001), and the Hyades moving group is typically associated with spiral structure (Quillen & Minchev 2005). Fig. 8 shows that for our sample, stars with similar kinematics to those of the Hyades and Hercules moving groups are seen in all metallicity bins and ages. However, we find that the central peak of the distribution for young stars shifts towards larger values of $-V_R$; V_ϕ as metallicity decreases. This shift in the peak of the kinematics of young stars may indicate that the relative contribution of each non-axisymmetric component of the disc (the spiral arms and bar, respectively) to the perturbed stellar kinematics varies as a function of metallicity. We note that this correlation also corresponds, as expected, to the observed metallicity gradient in the Galaxy (of the order $\partial[\mathrm{Fe/H}]/\partial R \sim -0.06$ dex kpc^{-1}; Boeche et al. 2013; Genovali et al. 2014).

The presence of young, metal-rich stars with similar kinematics as the Hyades moving group is consistent with the results of Quillen & Minchev (2005), Famaey et al. (2008), and Antoja et al. (2017),

who found the moving group to be metal rich and produced through gravitational interactions with spiral arms. In addition, the fact that we see these metal-rich stars visiting the solar neighbourhood from the inner disc, with similar kinematics as the Hercules moving group, suggests that these stars may have had their orbits affected by similar dynamical interactions with the central bar (Ramya et al. 2016; Antoja et al. 2017). Taking these points into account, we suggest that dynamical effects due to both the bar and spiral arms contribute to the steeper radial velocity gradient we find for young, metal-rich stars, while the more metal-poor stars are less affected by the bar. Our findings are then roughly consistent with Monari et al. (2017, see their fig. 4), where moving further from the OLR decreases the contribution of the bar, similar to what we find for our more metal-poor stars.

We also find secure results regarding the variation of V_ϕ with age, metallicity, and Galactocentric radius. All the old populations show a significant lag of V_ϕ relative to the circular speed, with little dependence on metallicity. Amongst the young stars, it is the most metal rich that shows the greatest lag in V_ϕ, which is a manifestation of the metallicity gradient in the thin disc and epicyclic motions of stars. The most metal-rich subsample of young stars shows rather surprising trends with R in both V_R and V_ϕ: its value for $\partial V_R/\partial R$ is much more negative than the values we obtain for the less metal-rich parts of the young sample, and its value for $\partial V_\phi/\partial R$ is strongly positive while the more metal-weak young stars show weakly negative values.

We find that the supersolar metallicity young stars have, on average, lower eccentricities than the supersolar metallicity old stars, pointing towards the possibility that the latter have migrated from much further in the Galactic disc. This result adds another dimension (age) to the findings of Kordopatis et al. (2015), where they show that super metal-rich (SMR) stars in the solar neighbourhood are on relatively circular orbits. They conclude that these SMR stars must be predominantly affected by resonant scattering at the OLR of the spiral arms (churning, Sellwood & Binney 2002), as their orbital angular momentum has increased to bring them to the solar neighbourhood, without a corresponding increase in eccentricity. We also note the bimodality in the eccentricity and guiding radius distributions for old, metal-rich stars, and suggest that this may be a possible signature of the different processes which bring them to the solar radius – either through epicyclic motions (i.e. stars with larger guiding radii which are temporarily visiting the solar neighbourhood) or churning (true migrators from the inner Galaxy).

With *Gaia* DR2 (Gaia Collaboration et al. 2018)[2] and additional individual chemical abundances (Wyse et al. in preparation), precise age estimates of these stars should allow for observational constraints on the relative efficiency of processes which bring them to the solar neighbourhood.

[2]https://www.cosmos.esa.int/web/gaia/dr2

REFERENCES

Adibekyan V. Z. et al., 2013, A&A, 554, A44
Antoja T., Figueras F., Torra J., Valenzuela O., Pichardo B., 2010, Lecture Notes Essays Astrophys., 4, 13
Antoja T., Figueras F., Romero-Gómez M., Pichardo B., Valenzuela O., Moreno E., 2011, MNRAS, 418, 1423
Antoja T. et al., 2015, ApJ, 800, L32
Antoja T. et al., 2017, A&A, 601, A59
Aumer M., Binney J., Schönrich R., 2016, MNRAS, 462, 1697
Bailer-Jones C. A. L. et al., 2013, A&A, 559, A74
Binney J., Tremaine S., 2008, Galactic Dynamics, 2nd edn. Princeton Univ. Press, Princeton, NJ
Binney J. et al., 2014, MNRAS, 437, 351
Boeche C. et al., 2011, AJ, 142, 193
Boeche C. et al., 2013, A&A, 559, A59
Bovy J., 2015, ApJS, 216, 29
Bovy J., 2017, MNRAS, 468, L63
Bressan A., Marigo P., Girardi L., Salasnich B., Dal Cero C., Rubele S., Nanni A., 2012, MNRAS, 427, 127
Carlin J. L. et al., 2013, ApJ, 777, L5
Carrillo I. et al., 2018, MNRAS, 475, 2679
Casagrande L., Schönrich R., Asplund M., Cassisi S., Ramírez I., Meléndez J., Bensby T., Feltzing S., 2011, A&A, 530, A138
Cutri R. M. et al., 2013, VizieR Online Data Catalog, 2328
De Silva G. M. et al., 2015, MNRAS, 449, 2604
Dehnen W., 2000, AJ, 119, 800
Famaey B., Pont F., Luri X., Udry S., Mayor M., Jorissen A., 2007, A&A, 461, 957
Famaey B., Siebert A., Jorissen A., 2008, A&A, 483, 453
Faure C., Siebert A., Famaey B., 2014, MNRAS, 440, 2564
Freeman K., Bland-Hawthorn J., 2002, ARA&A, 40, 487
Fux R., 2001, A&A, 373, 511
Gaia Collaboration et al., 2016, A&A, 595, A1
Genovali K. et al., 2014, A&A, 566, A37
Gilmore G. et al., 2012, Messenger, 147, 25
Gómez F. A., Minchev I., O'Shea B. W., Beers T. C., Bullock J. S., Purcell C. W., 2013, MNRAS, 429, 159
Górski K. M., Hivon E., Banday A. J., Wandelt B. D., Hansen F. K., Reinecke M., Bartelmann M., 2005, ApJ, 622, 759
Grand R. J. J., Kawata D., Cropper M., 2012, MNRAS, 421, 1529
Guiglion G. et al., 2015, A&A, 583, A91
Holmberg J., Nordström B., Andersen J., 2007, A&A, 475, 519
Kapteyn J. C., 1905, Rep. Br. Assoc. Adv. Sci., 264, 257
Kordopatis G. et al., 2011, A&A, 535, A107
Kordopatis G. et al., 2013a, AJ, 146, 134
Kordopatis G. et al., 2013b, MNRAS, 436, 3231
Kordopatis G. et al., 2015, MNRAS, 447, 3526
Kordopatis G., Wyse R. F. G., Chiappini C., Minchev I., Anders F., Santiago B., 2017, MNRAS, 467, 469
Kunder A. et al., 2017, AJ, 153, 75
Kushniruk I., Schirmer T., Bensby T., 2017, A&A, 608, A73,
Lee Y. S. et al., 2011, ApJ, 738, 187
Lindegren L. et al., 2016, A&A, 595, A4
Majewski S. R. et al., 2017, AJ, 154, 94
Matijevič G. et al., 2012, ApJS, 200, 14
McMillan P. J., 2013, MNRAS, 430, 3276
McMillan P. J. et al., 2018, MNRAS
Minchev I., Boily C., Siebert A., Bienayme O., 2010, MNRAS, 407, 2122
Monari G., Helmi A., Antoja T., Steinmetz M., 2014, A&A, 569, A69
Monari G., Famaey B., Siebert A., 2016, MNRAS, 457, 2569
Monari G., Famaey B., Fouvry J.-B., Binney J., 2017, MNRAS, 471, 4314
Nordström B. et al., 2004, A&A, 418, 989
Proctor R. A., 1869, Proc. R. Soc. I, 18, 169
Prusti T., 2012, Astron. Nachr., 333, 453
Purcell C. W., Bullock J. S., Tollerud E. J., Rocha M., Chakrabarti S., 2011, Nature, 477, 301
Quillen A. C., Minchev I., 2005, AJ, 130, 576
Quillen A. C., Dougherty J., Bagley M. B., Minchev I., Comparetta J., 2011, MNRAS, 417, 762
Ramya P., Reddy B. E., Lambert D. L., Musthafa M. M., 2016, MNRAS, 460, 1356
Recio-Blanco A. et al., 2014, A&A, 567, A5
Recio-Blanco A. et al., 2016, A&A, 585, A93
Rojas-Arriagada A. et al., 2016, A&A, 586, A39
Schönrich R., 2012, MNRAS, 427, 274
Schönrich R., McMillan P. J., 2017, MNRAS, 467, 1154
Schönrich R., Binney J., Dehnen W., 2010, MNRAS, 403, 1829
Schönrich R., Binney J., Asplund M., 2012, MNRAS, 420, 1281
Sellwood J. A., Binney J. J., 2002, MNRAS, 336, 785
Sharma S., Bland-Hawthorn J., Johnston K. V., Binney J., 2011, ApJ, 730, 3
Siebert A. et al., 2011, MNRAS, 412, 2026
Siebert A. et al., 2012, MNRAS, 425, 2335
Skrutskie M. F. et al., 2006, AJ, 131, 1163
Spagna A., Lattanzi M. G., Re Fiorentin P., Smart R. L., 2010, A&A, 510, L4
Steinmetz M. et al., 2006, AJ, 132, 1645
Widrow L. M., Gardner S., Yanny B., Dodelson S., Chen H.-Y., 2012, ApJ, 750, L41
Williams M. E. K. et al., 2013, MNRAS, 436, 101
Wojno J. et al., 2016, MNRAS, 461, 4246
Wojno J. et al., 2017, MNRAS, 468, 3368
Yanny B. et al., 2009, AJ, 137, 4377
Zhao G., Zhao Y.-H., Chu Y.-Q., Jing Y.-P., Deng L.-C., 2012, Res. Astron. Astrophys., 12, 723
Gaia Collaboration, Brown A. G. A., Vallenari A., Prusti T., de Bruijne J. H. J., Babusiaux C., Bailer-Jones C. A. L., 2018, preprint (arXiv:1804.09365)

[1]*Leibniz Institut für Astrophysik Potsdam, An der Sternwarte 16, D-14482 Potsdam, Germany*
[2]*Department of Physics and Astronomy, Johns Hopkins University, 3400 N. Charles St, Baltimore, MD 21218, USA*
[3]*Laboratoire Lagrange, Université Côte d'Azur, Observatoire de la Côte d'Azur, Boulevard de l'Observatoire, CS 34229, F-06304 Nice, France*
[4]*Lund Observatory, Lund University, Department of Astronomy and Theoretical Physics, Box 43, SE-22100 Lund, Sweden*
[5]*Rudolf Peierls Centre for Theoretical Physics, Keble Road, Oxford OX1 3NP, UK*
[6]*Observatoire astronomique de Strasbourg, Université de Strasbourg, CNRS, UMR 7550, 11 rue de l'Université, F-67000 Strasbourg, France*
[7]*Department FQA, Institut de Ciencies del Cosmos (ICCUB), Universitat de Barcelona (IEEC-UB), Marti Franques 1, E-08028 Barcelona, Spain*
[8]*Sydney Institute for Astronomy, School of Physics A28, University of Sydney, NSW 2006, Australia*

[9]*Astronomisches Rechen-Institut, Zentrum für Astronomie der Universität Heidelberg, Mönchhofstr. 12-14, D-69120 Heidelberg, Germany*
[10]*Faculty of Mathematics and Physics, University of Ljubljana, 1000 Ljubljana, Slovenia*
[11]*E.A. Milne Centre for Astrophysics, University of Hull, Hull HU6 7RX, UK*
[12]*Saint Martin's University, 5000 Abbey Way SE, Lacey, WA 98503, USA*
[13]*INAF National Institute of Astrophysics, Astronomical Observatory of Padova, I-36012 Asiago (VI), Italy*
[14]*Senior CIfAR Fellow, Department of Physics and Astronomy, University of Victoria, Victoria, BC V8P 5C2, Canada*

[15]*Department of Physics, Chong Yuet Ming Physics Building, The University of Hong Kong, Hong Kong*
[16]*Department of Physics and Astronomy, Macquarie University, Sydney, NSW 2109, Australia*
[17]*Western Sydney University, Locked Bag 1797, Penrith South, NSW 2751, Australia*
[18]*Mullard Space Science Laboratory, University College London, Holmbury St Mary, Dorking RH5 6NT, UK*

This paper has been typeset from a TEX/LATEX file prepared by the author.